Quantifying Trace Metals in Gunflint Microfossils by 3D Correlative X-ray Nanoimaging

Laurence Lemelle, Dmitry Karpov, Alexandre Simionovici, Lara Maldanis, Juan Fontecilla-Camps, Ana Diaz, Mirko Holler, Dario Ferreira Sanchez, Rémi Tucoulou, Peter Cloetens, et al.

▶ To cite this version:

Laurence Lemelle, Dmitry Karpov, Alexandre Simionovici, Lara Maldanis, Juan Fontecilla-Camps, et al.. Quantifying Trace Metals in Gunflint Microfossils by 3D Correlative X-ray Nanoimaging. Analytical Chemistry, 2026, ⟨10.1021/acs.analchem.5c07712⟩. ⟨hal-05577854⟩

HAL Id: hal-05577854

https://hal.science/hal-05577854v1

Submitted on 3 Apr 2026

analytical chemistry

Quantifying Trace Metals in Gunflint Microfossils by 3D Correlative X-ray Nanoimaging

Laurence Lemelle,[¶] Dmitry Karpov,[¶] Alexandre Simionovici,* Lara Maldanis, Juan C. Fontecilla-Camps, Ana Diaz, Mirko Holler, Dario Ferreira Sanchez, Rémi Tucoulou, Peter Cloetens, Wout De Nolf, Elisabeth Agnes Müller Gubler, Alain Manceau, Laurent Bonneviot, Kurt Konhauser,* and Russell Shapiro

Cite This: https://doi.org/10.1021/acs.analchem.5c07712

Read Online

ACCESS | Metrics & More | Article Recommendations | Supporting Information

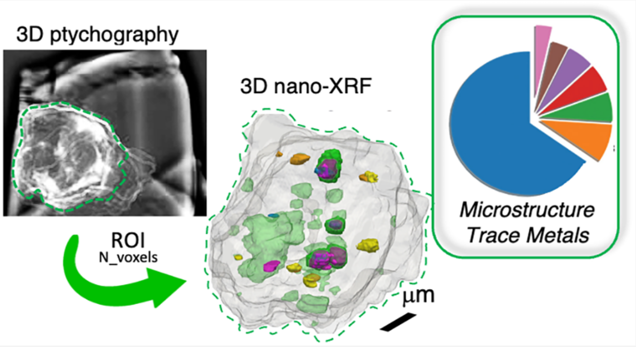

ABSTRACT: Probing elemental and structural heterogeneities is essential for understanding how materials evolve and degrade, yet correlating chemical and structural information across mesoscale specimens at the nanoscale remains analytically challenging. Here, we introduce a nondestructive correlative workflow that combines three-dimensional data sets from nanoscale X-ray ptychographic and fluorescence tomographies acquired on the same sample at dedicated synchrotron instruments. This workflow was developed and applied to quantify metal traces within individual low-Z compartments of a whole 1.88-billion-year-old Gunflint microfossil exhibiting a distinctive nanoscale architecture characteristic of thick-walled *Huroniospora*. Beyond the thick wall containing pluri-micrometer-sized quartz crystals with nanoinclusions, our analyses reveal an extracellular shell composed of submicrometer-sized quartz and Fe^{2+}-rich greenalite embedded within an Fe^{3+}-rich chert matrix. The specimen is unfractured and contains organic matter comparable to that of modern bacterial cells of similar volume. The trace sensitivity achieved in the multimetal three-dimensional maps, combined with precise volumetric quantification at nanometer scales, enabled accurate determination of metal concentrations in fossil compartments. Iron and manganese levels comparable to those of extant photosynthetic microorganisms, together with manganese−calcium-enriched iron silicate cores, suggest a cyanobacterial lineage and provide new insights into early microbial metabolisms. This correlative workflow, enabling high-sensitivity multielement trace analysis of low-Z nanostructured mesoscopic systems without physical subsampling, is broadly transferable to applications ranging from biominerals and geobiological materials to advanced functional materials such as catalysts, batteries, and nanocomposites.

■ INTRODUCTION

We present a correlative workflow combining nanoscale X-ray ptychographic and fluorescence tomographies that uniquely enables the quantification of metal traces of complex 3D nanostructures of low-Z mesoscale materials. Demonstrated on a microfossil, it is broadly applicable to other solid-state samples.

Elemental and structural heterogeneities at the nanoscale govern the fundamental properties and functions of materials—from catalytic activity and electronic performance to the preservation of primordial biological structures. Their analysis is, therefore, central to hard and soft materials science. Two-dimensional analytical techniques, while powerful, may fail to capture this information in complex three-dimensional systems, notably when chemical heterogeneities must be correlated with structure. Overcoming these limitations requires analytical strategies capable of volumetrically correlating the chemistry and structure at the nanoscale level. Electron microscopy can produce volumetric data, for example, through focused ion beam (FIB) serial sectioning. Still, its destructive nature, elemental sensitivity, and anisotropic resolution limit accurate analysis of trace elements of anisotropic materials and preclude subsequent analyses by other techniques. By contrast, X-ray computed tomography (CT) enables nondestructive volumetric imaging, adapted for rare or fragile samples.

Among CT-based techniques, X-ray fluorescence computed tomography (FXCT) stands out for its elemental sensitivity, allowing transition metals imaging of micrometer-scale targets

Received: December 5, 2025
Revised: March 1, 2026
Accepted: March 2, 2026

such as individual cells, mineral grains, or catalytic particles where self-absorption effects are minimal.[1−5] Optimally probing nanoscale fluorescence from transition metals fundamentally limits the achievable signal contrast for the low-Z elements. Multimodal 3D imaging methods combine X-ray fluorescence and ptychographic imaging to overcome this difficulty,[4,6−12] involving several trade-offs among sensitivity, resolution, and probing depth. In ptychography, for example, performance generally improves at lower X-ray energies because the coherence length, scattering efficiency, and diffraction angles increase as the energy decreases. In contrast, XRF experiments are optimized by tuning the incident beam energy to be at least 1−2 keV above the K absorption edge of the highest-Z element of interest by using a bright pink X-ray beam to maximize the total incident flux on the probed volume. Simultaneous data acquisition and alignment are performed, but they are particularly demanding when targeting both low-Z and high-Z elements at the nanoscale level. An improvement tailored for samples with low sensitivity to radiation consists of combining separately acquired elemental and structural data sets to optimize both the textural and trace-metal contrasts.

Here, we introduce a workflow for radiation-tolerant solids that was purposely designed to settle a challenging analytical issue in paleobiology. Trace contents of transition metals in microfossils have been proposed as promising proxies of metabolic activity[13] but remain difficult to quantify. Microfossils are pluri-micrometer-sized assemblages composed of insoluble organics and minerals exhibiting proper submicrometer heterogeneity. This complexity causes traditional two-dimensional XRF analyses for thin or infinitely thick layers to fail in accurately capturing the trace-metal inventory of the complete microfossils.[14] Such methods rely indeed on assumptions about geometry, volume, and elemental homogeneity, which limit their accuracy.[15−18] Optimal quantification requires sufficiently high excitation energy to access all relevant transition-metal lines, along with high photon flux and nanoscale 3D mapping of trace transition-metal distributions, coupled with structural reconstruction to precisely delimit the fossil volume precisely. High-Z trace-metal and low-Z contrasts from hard XRF are suboptimal to segment the silicified organic contours of a microfossil embedded within a silica matrix. Maximizing both low-Z textural and high-Z trace-metal contrasts becomes essential. To overcome this trade-off, we developed a workflow that integrates independently acquired data sets, enhancing both low-Z textural detail and trace-metal sensitivity.

For the development and validation of our workflow, we targeted thick-walled *Huroniospora* whole microfossils from the ca. 1.88 Ga Gunflint Formation at Schreiber Beach, Ontario,[19−21] commonly used as benchmarks in analytical advances for microfossil research. Under light microscopy, these appear as brown, carbonaceous spheroids (6−20 μm in diameter) with approximately 0.5-μm-thick walls, enclosing a dense mixture of low-maturity kerogen[22] and quartz microcrystals that contain heterogeneously distributed iron silicate and iron carbonate nanocrystals.[16,23,24] The metabolic implications inferred from the concentration of iron-rich nanocrystal[16] highlight the importance of accurately quantifying trace-metal content within entire microfossils.

We herein describe the developed workflow to perform a 3D correlative analysis of the content of trace transition metals throughout an entire thick-walled *Huroniospora* microfossil. Electron density 3D distributions from ptychographic X-ray computed tomography (PXCT), previously applied to other Gunflint specimens,[25,26] were here combined with 3D metal distributions from FXCT, compiled as in ref 27. Nondestructive synchrotron hard X-ray nanoprobes used were the cSAXS beamline at the Swiss Light Source for PXCT, and the ID16A beamline at the upgraded ESRF-EBS for XFCT. These provided, respectively, nanoscale structural and elemental data sets with optimal contrast. The postacquisition correlation of subcellular-resolution data across independent 3D data sets required the development of a dedicated workflow. This involved a dry preparation protocol to extract a single, intact microfossil, minimizing chemical contamination and making it suitable for repeated and complete 3D imaging. Complete structural characterization through high-resolution phase-contrast chromatography (PXCT) was first performed, followed by the acquisition of partial XRF information to identify markers in the sample using the same instrument. Subsequent high-sensitivity FXCT was performed on a dedicated high-energy, high-flux, high-resolution instrument. Alignment of the PXCT and FXCT data sets was then performed based on the XRF markers identified on both setups. Structural segmentation derived from PXCT data was then applied to the aligned FXCT data set to quantify the contents of trace metals within distinct subcompartments. This workflow provides whole-microfossil observables that are essential for evaluating cellular properties and their processing over geological time scales. Beyond microfossils, this workflow enables whole-object 3D analysis of low-Z solids bearing high-Z trace elements, necessary for understanding the element spatial distribution, chemical evolution, and performance-related properties from geobiology to materials science.

■ EXPERIMENTAL SECTION

FIB Sectioning

Two types of FIB sections were prepared: parallel sections for 2D XRF, nano-XRF and XANES ($x \times y \times z$: $\approx 5 \times 10 \times 3$ μm) and pillars (r; z: ≈ 5; 15 μm) for tomographic investigations, on a LYRA3 Tescan, operated at Tescan Analytics (Fuveau, France), and on an NVision40 Zeiss at EMF, PSI (Villigen, Switzerland). Delicate fossiliferous features were selected below the surface of submillimeter grains, obtained after dry-crushing plurimillimeter grains, using reflected light microscopy and fiducial marks (natural ones and carbon deposits) to eliminate the risk of surface contamination. Low ion currents and energies (at shallow angle steps in the final ion-polishing) were applied for the thin sectioning to prevent damage to the surface layer.

Synchrotron X-ray Ptychographic and Fluorescent Tomographies

PXCT was performed, under air, using the flOMNI instrument[28] at the cSAXS beamline of the Swiss Light Source. This beamline uses a fixed-exit double-crystal Si(111) monochromator with a central stop, a Fresnel zone plate with an outermost zone width of 60 nm, and an order-sorting aperture to deliver a coherent monochromatic beam of about 3.6×10^8 photons/s. Scattering is recorded by an in-vacuum Eiger 1.5 M CCD detector at 7.243 m from the sample. Data are iteratively inverted to obtain images of the sample with quantitative phase and absorption contrast.[29] 2D projections are subsequently aligned and reconstructed via tomography, as previously described.[30] Density values in g/cm^3 units were calculated using a simple model of electron density linked to the number of electrons per atom, using the following equation:

$$\rho = \frac{n_e A}{N_A Z}$$

where n_e is the electron density (electrons/cm^3), A is the molar mass (g/mol), N_A is Avogadro's number (mol^{-1}), and Z is the atomic number (total number of electrons in the atom). We note that this conversion to mass density in g/cm^3 assumes that the molecular composition of the material is known. However, for light elements, except H, the exact knowledge of the sample composition is not so stringent, since in this case $A/Z \approx 2$ g/mol.

High-resolution PXCT (≈50 nm) was collected out of focus, where the beam spot is 3.7 μm, at 6.2 keV, 280 single projections were acquired using a Fermat spiral position pattern scan (with a 0.5 μm step size). Additionally, low-resolution PXCT (voxel size ≈ 82 nm) and low-flux XRF tomography (voxel size ≈ 100 nm, 10^8 photons/s) were also simultaneously performed at the focus plane, where the spot size is about 100 nm, at 9.1 keV to provide an alignment reference for high-resolution PXCT and high-flux X-ray fluorescence tomography data sets. Fluorescence was detected with a KETEK H30 silicon drift detector (SDD) in combination with an XIA FalconX1 digital pulse processor. To obtain XRF volumes, 110 maps were acquired with 100 nm step size, 0.1 s dwell time, and a field of view of 10 μm × 4.8 μm (horizontal × vertical), over the range of angles from 0 to 360°.

High-flux X-ray fluorescence tomography was performed at the ID16A beamline of the European Synchrotron Radiation Facility Extremely Brilliant Source under high-vacuum conditions. The beamline uses a multilayer Kirkpatrick−Baez mirror system, which delivers a beam size of 23 nm (H) by 37 nm (V) with a flux of 4×10^{11} photons/s at 17.1 keV. Fluorescence is detected by multielement fast (≤1 Mcps) SDD detectors (7 elements Hitachi Vortex ME-7 SDD connected to XIA xMAP electronics and 16 elements ARDESIA-16 SDD connected to two XIA FalconX8 signal processors). The detectors were calibrated by using an AXO (AXO Dresden GmbH) RF8 thin film reference sample. To obtain XRF volumes, 96 high-resolution maps (with a step size of 50 nm and a dwell time of 50 ms) were acquired with a field of view of 10 by 5.3 μm^2 (horizontal x vertical), from 0° to 180°. The projections were then reconstructed at a voxel size ≈ 50 nm using the Filtered Back Projection algorithm implemented in the Nabu software developed at the ESRF (https://tomotools.gitlab-pages.esrf.fr/nabu/).

Combining PXCT with High-Flux XRF Tomography

The high-concentration Fe inclusions are well resolved on both the low- and high-flux 3D XRF maps. This allows finding the transformation to align two data sets using the triangulation of the Fe inclusions, which required precise identification of coordinates for individual inclusions using the center of mass approach. For the transformation, the low-flux data set was sampled up to match the voxel size of the high-flux data set. Next, we utilized the advantage that PXCT data were simultaneously collected with the low-flux XRF data set, resulting in the same coordinate space for the two data sets. Thus, we could transfer the rigid transformation found between low- and high-flux XRF to match the coordinates of the high-resolution PXCT data. To verify the quality of this alignment, we compared the centers of mass of high-density regions in the PXCT data set with the coordinates of the Fe inclusions in the high-flux XRF data set.

To access 3D spectral information, acquired XRF projections were tomographically reconstructed channel by channel. Each channel was aligned using the spatial shifts found during the alignment of the fitted Fe K$_\alpha$ line projections. The channel-by-channel reconstruction resulted in a 4D XRF data set (XYZ × Channels). To analyze the elemental distribution in different cell regions, we segmented the electron density maps obtained from PXCT. First, the segmentation was done by applying thresholding to the volume histogram. Then, the segmentation masks were manually refined, slice by slice, based on the local features. We then extracted spectra from individual 3D segmentation masks, by multiplying them with the 4D XRF data set and summing up voxels, thus preserving the channel information.

Synchrotron 2D XRF and XANES

Micro and nano-X-ray imaging were performed at the ESRF's ID21 and ID16B beamlines, respectively, which probe the elemental composition and speciation in the tender (2 to 9 keV) and hard (6−30 keV) X-ray energy regions. These undulator beamlines use fixed-exit double mirror systems for higher harmonic rejection, and fixed-exit double-crystal monochromators (Si 111, Kohzu Precision Co., Ltd., Japan) that deliver monochromatic beams with an energy resolution $\Delta E/E \approx 2 \times 10^{-4}$. The focusing procedure uses multilayer Kirkpatrick−Baez mirror systems which deliver beam sizes of 750 × 300 nm^2 (5×10^9 ph/s at 7.5 keV) or 50 × 60 nm^2 (5×10^{11} ph/s at 17 keV) for ID21 and ID16B, respectively. Fluorescence is detected by either single or multielement fast (≤1 Mcps) SDD detectors (Bruker XFlash 5100, 80 mm^2 area and 3 elements Hitachi Vortex-ME3 SDD 3 × 50 mm^2 and 7 elements MIRION SDD 7 × 50 mm^2 connected to XIA xMAP electronics), for ID21 and ID16B, respectively. Spectra are collected in "zap" continuous scanning mode by raster-scanning the sample in front of the focused beam while detectors continuously collect spectra. Maps provide raw counts of element lines per pixel, and when summed-up for regions of *Huroniospora* or the chert matrix, they yield high-statistics spectra for semiquantitative analysis parametrization. Fe K-edge XANES, spectra were acquired in the fluorescence mode in the energy range of 7.05−7.18 keV at 0.22 eV/step for ID21 and 7.05−7.3 keV and 0.5 eV/step, for ID16B, both calibrated against an Fe foil. Their edge energies were estimated by the maximum of the first derivative of the smoothed XANES scans with 0.15 and 0.25 eV uncertainties for ID21 and ID16B, respectively, and compared to references.[31] To improve their statistical quality without causing radiation damage, the multiple edge scans were combined: 60 at ID21 and 5 at the higher-flux ID16B. Sequential scans were verified to produce similar results, without changes indicative of radiation damage. We avoided collecting prepeak scans, which would have required approximately 10 times higher fluence for similar statistics. The edge energies were estimated by the maximum of the first derivative of the smoothed XANES scans with 0.15 and 0.25 eV uncertainties for ID21 and ID16B, respectively, and compared to references.[31] To minimize artifacts, each identified region was verified to yield consistent speciation across different flux levels, beam sizes, and sample preparations (Tables S1 and S2).

Statistics and Reproducibility

The relative count rate $\Delta_{i,n}$ of compartment i with respect to extracellular matrix n and its uncertainty $\sigma_{\Delta_{i,n}}$ are defined as

$$\begin{cases} \Delta_{i,n} = \dfrac{(S_i/N_i) - (S_n/N_n)}{(S_n/N_n)} \\ \sigma_{\Delta_{i,n}} = (\Delta_{i,n} + 1)\sqrt{\left(\dfrac{\sigma_{S_i}}{S_i}\right)^2 + \left(\dfrac{\sigma_{S_n}}{S_n}\right)^2} \end{cases}$$

where S, σ_S, and N designate the number of counts, their uncertainties, and the number of voxels, respectively, in the compartments. S and σ_S are the output of the PyMca fitting procedure.[32] As a measure of the fluorescence count rate reproducibility, the uncertainty of each pixel, subject to Poisson statistics, is the square root of the number of counts. The number of voxels N in a given compartment thus becomes an important parameter in order to quantify a $\sigma_{\Delta_{i,n}}$ value of the highest possible precision.

■ RESULTS AND DISCUSSION

Dry Preparation of Specimens

Our work involved labor-intensive development of a contamination-free preselection of specimens to ensure the integrity of subsequent analyses. Samples containing one individual specimen of *Huroniospora* were prepared from a stromatolitic chert—microcrystalline silica rock containing

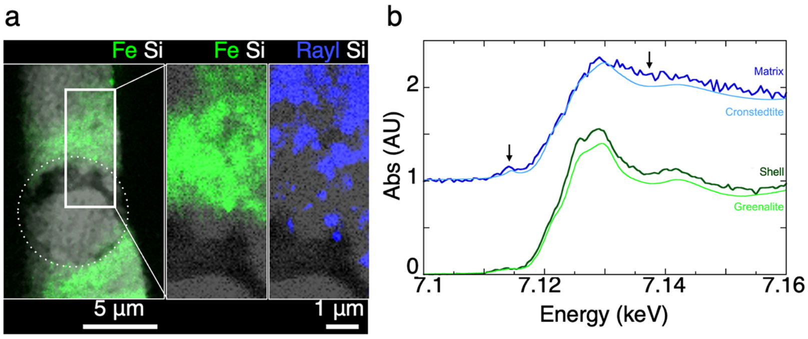

Figure 1. Cryptocrystalline hydrous Fe^{2+}-rich phyllosilicate fluffy extracellular shell. (a) Si, Fe fluorescence lines, and Rayleigh scattering maps (color-coded gray, green, and blue, respectively) from an FIB cross-sectioned microfossil (2.4 ± 0.2 μm thick, Figure S3a) recorded at 7.3 keV (dwell time: 0.2 s; pixel size: 500 nm; scale bar: 5 μm). The dotted white circle delineates the microfossil region. The white rectangle indicates a region depicted at its right at high resolution and sensitivity (dwell time: 0.5 s; pixel size: 50 nm; scale bar: 1 μm). (b) Average from nano-XANES spectra from the shell (green) and chert matrix (blue) in FIB cut sections. Micro-XANES from greenalite (light green) and cronstedtite (light blue) references.[34]

laminae rich in carbonaceous microfossils—collected at the Schreiber Beach locality (48.80° N, 87.34° W)[33] (Supporting text and Figure S1). To mitigate the risk of any potential trace contamination, submillimeter shards were first prepared through dry-crushing. We specifically chose the thinnest and darkest brown shards, which, as observed under transmission light microscopy, displayed numerous filaments and ovoid specimens, delineated by dark organic matter appearing in both clusters and isolated forms. We selected the darkest and largest carbonaceous spheroids (6−12 μm across), which were not yet visible in reflected light microscopy, despite the absence of optical polishing of the shard surface. These spheroids corresponded to the morphotype of well-preserved thick-walled *Huroniospora* specimens. The extraction step involved multiple microscopic markings and precise localization using multicontrast inspections by reflected light microscopy and scanning electron microscopy (SEM). All extractions were carried out using a Ga-focused ion beam coupled to an SEM (FIB-SEM) from the surface of the shard (see "Experimental Section" and Figure S2a). Pillars approximately 10 μm in diameter centered on single spheroids (Figure S2b) were prepared for tomography. Micrometer-thick sections were also prepared through the periphery of one spheroid (Figure S3) for high-sensitivity 2D analyses.

The validity of sample preparation and sample resistance to irradiation damage was preliminarily tested by performing high-sensitivity 2D synchrotron nano-XRF imaging (200 ms dwell time) on micrometer-thick FIB sections obtained from the periphery of thick-walled microfossils (see "Experimental Section" and Figure S3). Elemental maps of Si, Fe, and Ca, acquired at high signal-to-noise ratios and low spatial resolution (Figure 1a; Figure S4a; Figure S5a, left panel), revealed the thick wall as an irregular Si-depleted layer. Within the microfossil volume, micrometer-scale subeuhedral quartz crystals—hexagonal and elongated along the *c*-axis—appeared alongside Ca-rich inclusions adjacent to the wall, as previously observed by TEM.[23,24] The wall was enveloped in a "fluffy" Fe−Si-enriched shell several micrometers thick exhibiting a cryptocrystalline texture. This texture is consistent with the faint Fe background signal already detected in the ∼ 10 μm-thick peripheral shell of another *Huroniospora* microfossil.[16] At higher resolution (∼50 nm; Figure 1a, Figure S5a, right panel), the diffuse outer boundary of this shell appeared intricately interwoven with 200−500 nm quartz crystallites, identifiable in the Rayleigh scattering image due to its enhanced low-Z sensitivity. In agreement with the microquartz texture characteristic of the surrounding chert matrix,[24] both the size and density of these quartz crystallites increase with their distance from the microfossil surface.

The chemical forms of Fe were identified by Fe K-edge nano-XANES (beam size ca. 60 nm; see "Experimental Section" and Figure 1b, Figures S4−S6b). They closely resemble greenalite, a $^{VI}Fe^{2+}$ phyllosilicate found in the well-preserved Fe-rich external shell, and cronstedtite, a non-stoichiometric $^{VI}Fe^{2+}$-$^{VI}Fe^{3+}$-$^{IV}Fe^{3+}$ phyllosilicate, present in the chert matrix (Figure S6, Table S1). The concordant Fe speciation results previously obtained with different beam sizes, intensities, and sample preparation methods[35] (Table S2) support the reliability of the sample preparation protocol. They also confirm minimal radiation-induced alteration during faster 3D scanning, and transition-metal detection in our CT performed at a comparable integrated count rate at higher incident energies.

3D Distributions of the Phases

To select the best-preserved microfossil, we applied synchrotron-based PXCT at ∼50 nm resolution to three custom-made 3D FIB pillars (Figure S2), each containing a carbonaceous structure expected to be a microfossil. This enabled the assessment of a classical suite of macroscopic features. There were no fractures, whose presence may reflect later oil circulation.[36] Organics were found within an ovoid. This is consistent with early silica encapsulation that occurred during life or shortly after death, when cytoplasm was still present.[20,37] We surveyed internal textures across and around the specimens using a model linking the electron density to the mass density following an established quantification method[38] (see "Experimental Section"). The 3D distributions distinguished three phases: kerogen (1.40 ± 0.16 g/cm^3) and silica, likely as quartz, (2.60 ± 0.04 g/cm^3 in the microfossil and 2.57 ± 0.07 g/cm^3 in the chert matrix), from air (see "Experimental Section" and Figure S2c) consistent with previous analyses.[25] Two pillars contained one ovoidal structure (Figure S2b), which contained micrometer-sized subeuhedral quartz crystals surrounded by kerogen. The microfossil kerogen walls bear the imprint of both the internal crystals and the external equant submicrometer matrix crystals.[23,24] Consequently, the walls display a variable thickness ranging from 0 to 600 nm. They appear continuous and thick in the summed PXCT z-

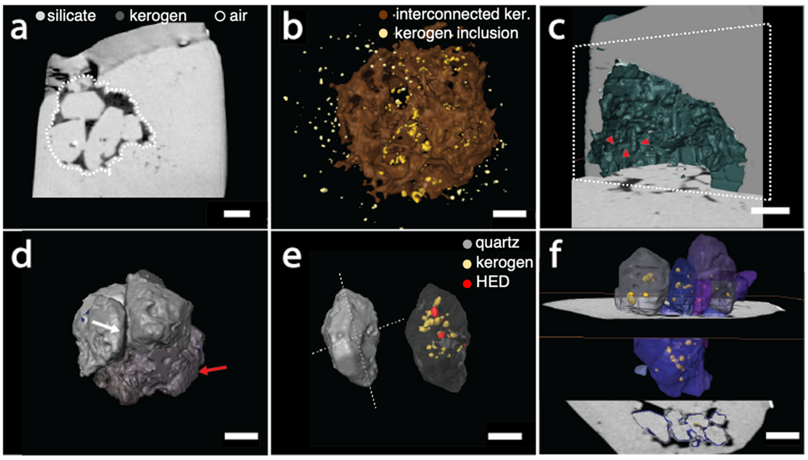

Figure 2. Texture of the selected *Huroniospora* specimen. (a) Tomographic virtual slices cut across a microfossil within the rock sample. The white dotted line outlines the microfossil contours. (b) 3D rendering of the interconnected organics (brown) and isolated organics in the microfossil (orange) and outside (yellow). (c) 3D rendering of the matrix minerals that encase the organics of the microfossil. (d) View of the intramicrofossil minerals displaying a few micrometer-sized quartz crystals with large contact facets (white arrow) and a compact quartz assemblage (red arrow). (e) An enlarged view of a typical subequant quartz surface with 120° angles and symmetry imposed by the vertical 3-fold and horizontal 2-fold axes. The crystal contains several nanometer-sized inclusions of low (yellow) and high (red) density. (f) Magnified assemblage of the minerals shown in (d), composed of small quartz crystals whose contours are outlined in blue in the bottom gray section view. Scale bars: 1 μm.

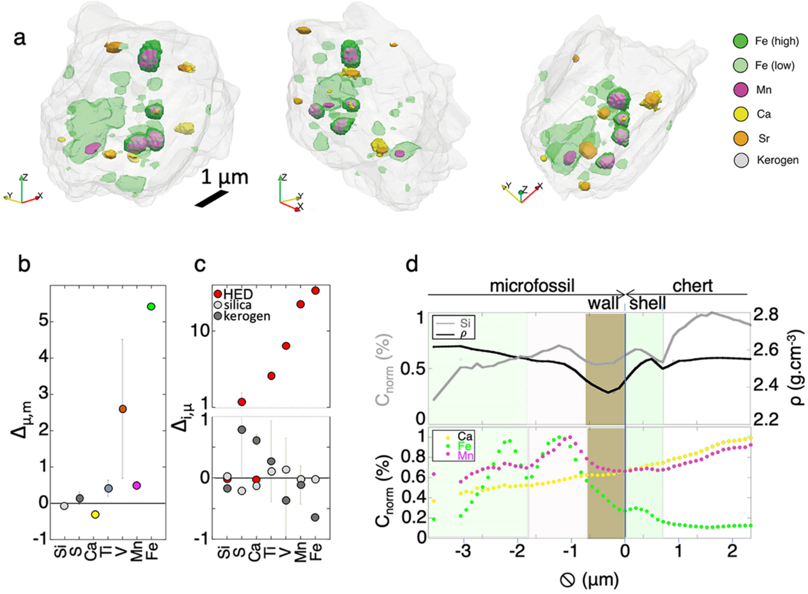

Figure 3. Trace metals within the selected *Huroniospora* specimen. (a) Reconstructed Fe- and Ca-rich volumes within the best-preserved microfossil from XRF-CT data, superimposed on the aligned PXCT volume of the organics, are shown from three different perspectives. Scale bar: 1 μm. (b) The relative count rates of the elemental concentrations $\Delta_{\mu,m}$ of the microfossil compartment "μ" with respect to those of the extracellular matrix compartment "m". (c) The relative count rates of the elemental concentrations $\Delta_{i,\mu}$ of one of the three compartments "i" distinguished by PXCT (≈13.7 vol % of organics (gold), ≈0.8 vol % μm^3 of HED inclusions (red), ≈85.5 vol % μm^3 of silica (gray) in the full 145.8 μm^3 microfossil) with respect to those of the microfossil "μ". The *y*-axis is on a linear scale before the break and on a log scale above it. Error bars, when not seen, are smaller than the circles and correspond to uncertainties defined in "Experimental Section". (d) (Top) Radial Si and density distributions (gray and black lines, respectively); the Si-depleted and less dense kerogeneous wall (brown compartment) and the 2.57 ± 0.07 g/cm^3 chert matrix (white) are highlighted; (bottom) Fe (green), Ca (yellow), and Mn (pink) profiles displaying the extracellular Fe-rich shell and the intracellular cortical Mn-rich layer and Fe-rich core. Corresponding error bars indicating the variation within the masks used for the calculation are depicted in Figure S9.

projections of the microfossil, which was fully sampled within the pillar (Figure 2a). They closely match the distinctive morphological traits of thick-walled *Huroniospora* observed in visible microscopy. This sample was subsequently selected for further analyses (Figure S2 a3 and b4-7-10).

The texture of the selected sample was quantitatively assigned to the four classes of compartments defined below based on kerogen density, quartz density, low electron density (LED), and high electron density (HED), all determined using the same method.[38]

The 3D rendering of the kerogen density (1.40 ± 0.16 g/cm^3) distribution of this microfossil (Figure 2b) reveals an interconnected lattice of organics (~20.7 μm^3) between quartz crystals. This lattice defines the spheroidal volume of the microfossil (~145.8 μm^3). There are also several isolated organic inclusions measuring less than 500 nm inside the intracellular quartz crystals. External organic inclusions appear smaller than their intracellular counterparts and are found within 1 μm from the microfossil surface (Figure 2b). The organic volume of the microfossil corresponds to about 14% of its full volume. At the outer interface with the chert matrix, the virtual mold of the organics exhibits finely faceted nanograins, each approximately 100 nm in length (Figure 2c).

The 3D rendering of quartz density (2.57 ± 0.07 g/cm^3) demonstrates a compact intracellular assemblage of hexagonal micrometer-sized subeuhedral quartz crystals, elongated in their *c*-axis direction (Figure. 2d,e). There are also loosely shaped aggregates made of smaller quartz crystals that follow the internal contours of the microfossil (Figure 2f). Ill-defined facets appear in the periphery of the internal interface between the microfossil wall and the intracellular volume. The subeuhedral crystals encase 100-nm sized inclusions (Figure 2e,f), with densities that can either be low (LED, 1.40 ± 0.16 g/cm^3) or high (HED, 2.68 ± 0.16 g/cm^3), consistent with kerogen (1.40 ± 0.16 g/cm^3) and iron silicate or iron carbonate nanocrystals (3 ± 0.15 g/cm^3), respectively. The heterogeneous density distribution, likely linked to local variations in Fe concentration, highlighted the need to quantify metal concentrations across the microfossil.

The superposition of the 3D reconstructions of the four classes of compartments reveals an intricate internal texture. The outer envelope surrounding the kerogen lattice defines the microfossil's spheroidal shape, consistent with a biological origin of the structure. Localized loss of structural integrity, similar to the internal displacement of kerogen during quartz growth, is evident, even in 2D PXCT views. However, a complete 3D survey of the microfossil shows a discontinuous yet concentric coarse-grained symmetry. This comprises a central compact quartz assemblage, smaller quartz crystals conforming to the internal contours of the microfossil wall, a spheroidal discontinuous wall, finely faceted nanograins on the outer wall surface, and the surrounding matrix; this, in turn, raises the question of the level of structural loss. Phase volumes within the microfossil provide key observables on this scale. Assuming the kerogen volume reflects the original cellular organic volume (density ≈ 1.4 g/cm^3), and the remaining volume (~125.8 μm^3) corresponds to cytoplasmic water volume, the organic mass fraction is estimated at 17.5% by weight. Under conservative uncertainty assumptions (2.5% on volume; ± 0.1 g cm^{-3} on density), uncertainty is <1 wt %, and dominated by the density uncertainty. This value closely matches predictions for extant bacteria derived from the functional allometric relationship between dry weight and volume.[39] Although localized structural degradation is evident, 3D reconstructions based on averaged electron density do not exclude the preservation of cellular organic matter and aspects of its concentric organization during the first fossilization steps, providing a framework for correlating PXCT with FXCT analyses.

3D Distributions of the Metals in the Microfossil Texture

Three-dimensional elemental distributions (Figure 3a) were obtained at a voxel size of 50 × 50 × 50 nm^3 for our best-preserved specimen (see Experimental Section). For quantitative analysis, the fluorescence spectra were fitted using the open source PyMCA program.[32] The fundamental parameters of the experimental setup were calibrated using a thin film standard (AXO Dresden) measured under conditions identical with those of the sample (see Experimental Section and Tables S3 and S4). Accurate alignment (see Experimental Section, Figure S7) of the FXCT and PXCT data sets within half a voxel was determined from the iron map of a 2D transverse section of the pillar containing HED inclusions. This section was compiled from a low-sensitivity FXCT data set simultaneously acquired simultaneously with the PXCT scan, and the investigated high-sensitivity FXCT data set obtained at beamline ID16A (Figure S8). The 3D rendering of elemental volumes superimposed on the aligned PXCT volume of the organics is shown from three different perspectives (Figure 3a). They display three submicrometer Fe-rich volumes correlated with Mn-rich volumes, ~ 10 times smaller Ca-rich volumes correlated with Sr volume and preferentially located near the wall, and diffuse irregular Fe-bearing volumes with lower Fe concentrations than the Fe-rich volumes.

We calculated relative count rates to quantitatively compare elemental concentrations across different parts of the sample without relying on complex normalization. The unitless relative count rate of compartment "*i*" with respect to that of a reference "*r*" was defined as $\Delta_{i,r} = \frac{(S_i / N_i) - (S_r / N_r)}{(S_r / N_r)}$, where *S* designates the number of counts and *N* is the number of voxels in a compartment (the corresponding uncertainties are detailed in the "Experimental Section" section). Reference was either the extracellular chert matrix (contrast denoted as Δ_m) or the whole microfossil (contrast denoted as Δ_μ). XRF-CT data sampling was conducted by applying a binary mask derived from the PXCT data set, following the conventional method of pixel-wise normalization. Two strategies were employed to analyze the chemical concentration distributions: (i) averaging within the density-defined compartments identified by PXCT (the microfossil, the organic lattice, the "silica-rich" regions, and the "HED" inclusions, Table S3) and (ii) averaging within concentric shells from the microfossil surface. The mesoscale outcomes that can be obtained from these two types of nanoanalysis averages are illustrated in detail below for the selected microfossil specimen.

Average within the Density-Defined Compartments Identified by PXCT. Relative to the quartz extracellular matrix, the microfossil exhibits a slight depletion of Si (Δ_m ≈−0.07 ± 0.001 in Figure 3b), a high enrichment in Fe (Δ_m ≈ 5.44 ± 0.03 in Figure 3b), and to a lesser extent, enrichment in V, Mn and Ti ($0.4 < \Delta_\mathrm{m} < 2.5$ in Figure 3b). Using the Fe concentration of ~1.5 × 10^6 atoms μm^{-3} reported for the chert matrix by Lepot et al.,[16] and considering an uncertainty of ±0.1 × 10^6 atoms μm^{-3}, an Fe density of 9 ± 1 × 10^6 atoms μm^{-3} in the microfossil is inferred from the value extrapolated using the relative contrast. Using the Fe/Mn ratio (≈150; Table S4), it corresponds to an Mn density exceeding 5 × 10^4 atoms μm^{-3}.

Relative to the whole microfossil, the organics compartment (Figure 2b) has less Si (Δ_μ ≈ −0.16), Fe, and V but is enriched in Ca (Δ_μ ≈ 0.62 ± 0.009) and slightly in S (Figure 3c). This enrichment may be attributed to colocalized calcium sulfates and organic sulfides within the kerogens (Figure 3a).[22] Due to the relatively small volume of the organics compartment (≈13.7 vol %) and low negative fractionation values for Fe, V, and Mn (Δ_m ≤ 0), this compartment does not significantly contribute to the detected enrichment of Fe, V, and Mn within the microfossil.

The HED inclusion rendering (Figure 2f) shows the highest trace-metal enrichments (Figure 3c), in particular, in Fe (Δ_μ ≈

35). However, due to the small volume of the HED compartments (≈0.8% vol), this compartment does not significantly contribute to the detected Fe-enrichment of the microfossil. Such enrichment is observed in the less concentrated but considerably larger intracellular silica compartment (Table S3). It may be due to the presence of Fe silicate and/or Fe carbonate nanocrystals encased within the quartz crystals that are too small to be detected by PXCT (Figure 2e,f). Manganese is also present in excess within the HED inclusions, which are only 1.4 times richer in Fe than in Mn (Figure 3c); this is in contrast to the whole microfossil, where this ratio is approximately 10 (Figure 3b). Mn-rich cores (pink in Figure 3a) were identified within some of the more Fe-rich precipitates (dark green in Figure 2a). These specific Mn-rich cores are also associated with Ca but close to the detection limit (Table S4).

Average within Concentric Shells from the Microfossil Surface. In parallel with analyses of the density compartments, spheroidal distributions of elemental and electron density (ED) were obtained by averaging XRF and PXCT signals across 100-nm thick layers nested around the external surface of the ovoid microfossil (Figure 3d, Figure S9). We observe a 0.5−1.0 μm thick organic shell with low electron density and Si concentration characteristic of thick-walled *Huroniospora*. It is overlain by an ~1 μm-thick Fe−Si-enriched shell embedded in a silica matrix of uniform composition. Notably, while the average ED shows no detectable internal contrast within this shell, metal concentrations do. Beneath the wall, an approximately 1 μm-thick Si−Fe−Mn-rich shell encloses a core relatively enriched in Fe and depleted in both Si and Mn. The average bulk density of approximately ~1 μg Fe/mm^3 within the microfossil (Figure S9) corresponds to ~10^7 Fe atoms/μm^3 providing an alternative estimation consistent with that previously obtained from Δ_m analyses using the chert matrix value reported by Lepot et al.[16] The apparent gradual decrease in Ca concentration toward the center of the microfossil is an artifact except for the increase just detectable below the wall, which reflects uncorrected fluorescence self-absorption in the pillar. While the uncertainty of the composition measurement is better than 1% for transition metals, that of the Ca composition varies from 100% at the core to 36% at the periphery. This difference arises from two dominant sources of uncertainty: self-absorption of fluorescence photons and photon-counting statistics for lower-concentration elements. Self-absorption is more pronounced for lighter elements (here Ca), while for transition metals with K-line energies above ~ 6 keV it remains modest at the ~10 μm thickness of our specimen, though it would increase for larger or denser samples.[3] Photon-counting noise limits the detectability of Mn and Ca, whose voxelwise signals approach the background. The signal-to-noise ratio improves with the square root of the number of integrated voxels and eventually saturates at a value determined by the size of the studied compartment.

■ DISCUSSION

Our combined PXCT−FXCT workflow captures the three-dimensional distributions of transition metals across the entire object, with no subsampling or extrapolation inaccuracies, overcoming long-standing analytical limitations. The full workflow comprises the segmentation of the ptychographic volume, spatial virtual resampling to match the XRF voxel resolution, application of the ptychographic mask to the hyperspectral data set, XRF spectral fitting on the reduced data, and integration of elemental concentrations within each segmented region.

The analysis performed through our methodology yielded bulk metal concentrations robustly supported by direct, comprehensive quantification without sampling or extrapolation. As shown in previous studies, the bulk concentration of metals provides crucial insights into cellular metabolism, particularly for Fe, the most abundant transition-metal trace in *Huroniospora* microfossils. The value between 8 and 10 × 10^6 iron atoms·μm^{-3} (regardless of the estimation method applied) is 1−2 orders of magnitude above that of most nonphotosynthetic bacteria.[40,41] It is typical of cyanobacteria[42] and anaerobic green sulfur bacteria,[43,44] which require elevated Fe levels to sustain their abundant photosystem I with its three [Fe_4S_4] clusters or diazotrophs for the [Fe−S] clusters of nitrogenase.[45] Our estimate is significantly lower than the values extrapolated from 2D electron microscopy (>10^8 Fe atoms·μm^{-3}) where Fe-rich nanocrystals have been more finely characterized in shape and composition, but only over a fraction of the total cell volume. Our method obviates detailed 2D heterogeneity characterization by directly addressing the overall elemental variability.

The enhanced sensitivity of our methodology additionally allowed quantification of less abundant transition metals, providing additional constraints to refine the interpretations of early metabolisms. The estimated Mn concentration value exceeded 5 × 10^4 Mn atoms·μm^{-3}. This value is within the range reported for extant cyanobacteria (2−5 × 10^5 Mn atoms·μm^{-3}),[46] and 1−2 orders of magnitude higher than typical concentrations in present-day photosynthetic green sulfur bacteria.[46,47] The agreement of the estimated Mn atoms per cell with that of cyanobacteria is notable. Indeed, these organisms require Mn to sustain the specific [Mn_4CaO_5] cluster of their abundant photosystem II, the catalytic core of water oxidation and oxygen production. These high Mn and Fe bulk concentrations are consistent with those measured on clusters of mixed *Gunflintia* and *Huroniospora* microfossils from Schreiber Beach, by destructive depth profiling using mass spectrometry at 20 μm resolution.[48] Determining whether the Mn−Ca pattern is a primary cellular signal or a secondary overprinted signal is beyond the scope of this methodological study and will be the subject of future studies.

These discussions illustrate that beyond bulk averaging of metal traces in the virtually segmented whole object, their quantification across complex 3D nanostructures at multiple scales provides a unique means to trace their origin and their reprocessing. Although only a limited number of specimens can currently be analyzed using ultraresolved and ultrasensitive 3D methods, our workflow, through precise alignment and segmentation of independently acquired data sets, allows for 3D mapping of sub-100 nm-scale heterogeneities and bulk elemental inventories within complex microstructures. This approach overcomes the limitations of traditional 2D, or sampling-based, destructive methods. Self-absorption of fluorescence photons and photon-counting statistics will dictate the precision in most low-Z nanostructured systems. Analytical or iterative self-absorption corrections methods[3,49,50] can partially recover accuracy for fluorescence lines, though the effectiveness diminishes with specimen thicker than their typical X-ray attenuation length (<100 μm for transition metals). Gains in detector solid angle and energy resolution will directly lower the photon-noise background, while data processing strategies such as principal component spectral decomposition or self-supervised denoising of low-count XRF maps[51] offer alternatives to improve signal extraction without longer acquisitions, higher doses, or hardware changes. Our 3D analyses may then be combined with 2D workflows optimized for cross-investigation of rock-hosted organic matter over extended fields of view.[52]

Beyond microfossils, our workflow provides a transferable strategy for nondestructive, high-resolution characterization of heterogeneous materials in geobiology, catalysis, battery research, and nanomaterials science. Examples of applications include resolving metal cofactor compartmentalization in cells and biominerals, tracking nanoparticle redistribution in heterogeneous catalyst supports, mapping heavy dopant and metal impurity distributions in silicon-based semiconductor architectures, and characterizing transition-metal migration in polymer-bound battery electrodes. These systems share a common analytical challenge: detecting trace high-Z elements embedded in low-Z matrices whose three-dimensional structure must be appraised to interpret the chemistry. The workflow is directly applicable, provided that the specimen tolerates the required radiation dose and can be accommodated within the field of view of current nanoprobe instruments.

CONCLUSIONS

This study demonstrates the capability of correlative, nondestructive PXCT−FXCT nanoimaging to resolve the three-dimensional distribution of transition metals within whole ancient microfossils. By integrating electron density and elemental information at the submicrometer scale, this approach enables simultaneous identification of localized metal (high-Z trace) enrichments, such as Fe−Mn−Ca-rich inclusions, and reconstruction of bulk (low-Z major) compositional patterns previously inaccessible through single-modality techniques. Here, both absolute elemental concentrations and relative count rates between distinct structural compartments were established. The latter also allows for extrapolation of absolute contents if one compartment has a known concentration.

Applied to a 1.88-billion-year-old *Huroniospora* microfossil, our workflow yielded robust, full-volume quantifications of Fe (8×10^6 atoms·μm^{-3}) and Mn ($>5 \times 10^4$ atoms·μm^{-3}). These elevated metal quotas align with those of extant cyanobacteria, supporting an oxygenic photosynthetic metabolism and highlighting trace-metal inventories as durable biosignatures of early life—more resilient than morphology alone, over geological time scales. Several other trace metals (V, Cu, Zn, W) that potentially play key roles in cell metabolism as cofactors were also quantified, offering complementary information to evaluate the metabolic inference.

Beyond paleobiology, our developed workflow, which combines precise 3D alignment, high-resolution multimodal imaging, and large-scale FIB-based whole-sample preparation, provides a generalizable framework for analyzing nanoscale heterogeneities and macroscopic compositional trends of high-Z traces in complex low-Z solid materials. Its applicability will extend to diverse fields that investigate heterogeneous solid materials with low sensitivity to radiation damage. These include disciplines ranging from early life detection and environmental science to advanced nanoelectronic material analysis.

ASSOCIATED CONTENT

Supporting Information

The Supporting Information is available free of charge at https://pubs.acs.org/doi/10.1021/acs.analchem.5c07712.

> Additional sample details (provenance, petrographical section, shards); photograph of Schreiber Beach microfossiliferous material (Figure S1); ptychographic data and column preparation views (Figure S2); XANES cross-section preparation views (Figure S3); XANES maps and spectra (Figures S4−S6); XRF data with raw spectra of the structure and substructures (Figure S7); schematic of the combined tomography workflow (Figure S8); elemental radial profiles (Figure S9); tables of XANES spectral deconvolution parameters (Table S1), Fe K-edge XANES acquisition conditions (Table S2), K-line analyses of elements detected in summed XRF spectra (Table S3); and raw Fe, Mn, and Ca counts detected in the three HED "i" clusters (Table S4) (PDF)

AUTHOR INFORMATION

Corresponding Authors

Alexandre Simionovici − *ISTerre, Univ. Grenoble Alpes, Univ. de Savoie Mont Blanc, CNRS, IRD, IFSTTAR, 38058 Grenoble, France;* orcid.org/0000-0001-5349-6482; Email: alexandre.simionovici@univ-grenoble-alpes.fr

Kurt Konhauser − *Department of Earth and Atmospheric Sciences, University of Alberta, Edmonton, Alberta T6G 2E3, Canada*; Email: kurtk@ualberta.ca

Authors

Laurence Lemelle − *LGL-TPE, ENS de Lyon, Univ. de Lyon, CNRS, 69364 Lyon, France;* orcid.org/0000-0002-7082-5564

Dmitry Karpov − *Swiss Light Source (SLS), Paul Scherrer Institute, 5232 Villigen PSI, Switzerland; ESRF - The European Synchrotron, ID16A/ID16B/ID21 Beamline, 38043 Grenoble, France;* Present Address: Université Grenoble Alpes, CEA, IRIG, MEM, NRX, Grenoble, 38054, France; orcid.org/0000-0001-5095-7300

Lara Maldanis − *ISTerre, Univ. Grenoble Alpes, Univ. de Savoie Mont Blanc, CNRS, IRD, IFSTTAR, 38058 Grenoble, France;* orcid.org/0000-0001-8835-4679

Juan C. Fontecilla-Camps − *Institut de Biologie Structurale, Univ. Grenoble Alpes, CEA, CNRS, 38000 Grenoble, France;* orcid.org/0000-0002-3901-1378

Ana Diaz − *Swiss Light Source (SLS), Paul Scherrer Institute, 5232 Villigen PSI, Switzerland;* orcid.org/0000-0003-0479-4752

Mirko Holler − *Swiss Light Source (SLS), Paul Scherrer Institute, 5232 Villigen PSI, Switzerland;* orcid.org/0000-0001-8141-0148

Dario Ferreira Sanchez − *Swiss Light Source (SLS), Paul Scherrer Institute, 5232 Villigen PSI, Switzerland*

Rémi Tucoulou − *ESRF - The European Synchrotron, ID16A/ID16B/ID21 Beamline, 38043 Grenoble, France;* orcid.org/0000-0002-8038-5275

Peter Cloetens − *ESRF - The European Synchrotron, ID16A/ID16B/ID21 Beamline, 38043 Grenoble, France*

Wout De Nolf − *ESRF - The European Synchrotron, ID16A/ID16B/ID21 Beamline, 38043 Grenoble, France*

Elisabeth Agnes Müller Gubler − *Electron Microscopy Facility, Paul Scherrer Institute, 5232 Villigen PSI, Switzerland*

Alain Manceau − *Laboratoire de Chimie, ENS de Lyon, Univ. de Lyon, CNRS, 69342 Lyon, France;* orcid.org/0000-0003-0845-611X

Laurent Bonneviot − *Laboratoire de Chimie, ENS de Lyon, Univ. de Lyon, CNRS, 69342 Lyon, France;* orcid.org/0000-0002-9092-8966

Russell Shapiro − *Department of Geological and Environmental Sciences, California State University Chico, Chico, California 95929-0205, United States*

Complete contact information is available at: https://pubs.acs.org/10.1021/acs.analchem.5c07712

Author Contributions

¶L.L. and D.K. contributed equally to this work. Sample preparation: L.L., R.S., E.A.M.G., and D.K.; Ptychography: D.K., A.D., M.H., L.M., L.L. and A.S.; XANES: A.S., W.D.N., L.L., D.F.S., R.T., A.M., and L.B.; 3D XRF: D.K., P.C., L.L., and A.S.; Funding acquisition: L.L., A.S., A.D., P.C., and R.T.; Project administration: L.L. and A.S.; Supervision: L.L. and A.S.; Writing—original draft: L.L., A.S.,. L.B., A.M., D.K., K.K., J.C.F.-C., and R.S.; Writing—review and editing: all authors.

Notes

The authors declare no competing financial interest.

■ ACKNOWLEDGMENTS

This research was supported by a Metallome CNES grant, by the Swiss National Science Foundation grant number 200021_175905, and by the French National Research Agency in the framework of the Investissements d'Avenir program (ANR-15-IDEX-02). We are grateful to the ESRF-EBS facility (Proposals ES521, ES677, ES937, MI1231 and commissioning beamtime BLC13299) and the PSI facility (Proposal 20182104).

■ DEDICATION

⋈Institut Universitaire de France (IUF).

■ REFERENCES

(1) Simionovici, A. S.; Lemelle, L. GGR Handbook of Rock and Mineral Analysis Chapter 16 Nano-Imaging for Advanced X-Ray Fluorescence and Absorption Spectroscopy Applications. *Geostand. Geoanalytical Res.* **2025**, *49* (3), 495−533.

(2) De Samber, B.; Meul, E.; Laforce, B.; Paepe, B. D.; Smet, J.; Bruyne, M. D.; Rycke, R. D.; Bohic, S.; Cloetens, P.; Coster, R. V.; Vandenabeele, P.; Berghe, T. V. Nanoscopic X-Ray Fluorescence Imaging and Quantification of Intracellular Key-Elements in Cryofrozen Friedreich's Ataxia Fibroblasts. *PLoS One* **2018**, *13* (1), No. e0190495.

(3) Bleuet, P.; Gergaud, P.; Lemelle, L.; Bleuet, P.; Tucoulou, R.; Cloetens, P.; Susini, J.; Delette, G.; Simionovici, A. 3D Chemical Imaging Based on a Third-Generation Synchrotron Source. *TrAC Trends Anal. Chem.* **2010**, *29* (6), 518−527.

(4) Deng, J.; Lo, Y. H.; Gallagher-Jones, M.; Chen, S.; PryorJr, A.; Jin, Q.; Hong, Y. P.; Nashed, Y. S. G.; Vogt, S.; Miao, J.; Jacobsen, C. Correlative 3D X-Ray Fluorescence and Ptychographic Tomography of Frozen-Hydrated Green Algae. *Sci. Adv.* **2018**, *4*, No. eaau4548, DOI: 10.1126/sciadv.aau4548.

(5) Simionovici, A.; Lemelle, L. X-Rays Analysis for Space Sciences: X-Ray Fluorescence Spectroscopy. In *Encyclopedia of Analytical Chemistry*; John Wiley & Sons, Ltd, 2018; pp 1−31 DOI: 10.1002/9780470027318.a9649.

(6) Vanpeene, V.; Stamati, O.; Guilloud, C.; Tucoulou, R.; Holliger, B.; Chandesris, M.; Lyonnard, S.; Villanova, J. Comparative Study of the Quantitative Analysis of Battery Materials with X-Ray Nano-Tomography: From Ex Situ toward Operando Measurements. *ACS Nano* **2025**, *19*, 9994.

(7) Liu, Y.; Meirer, F.; Krest, C. M.; Webb, S.; Weckhuysen, B. M. Relating Structure and Composition with Accessibility of a Single Catalyst Particle Using Correlative 3-Dimensional Micro-Spectroscopy. *Nat. Commun.* **2016**, *7* (1), No. eaau4548.

(8) Meirer, F.; Morris, D. T.; Kalirai, S.; Liu, Y.; Andrews, J. C.; Weckhuysen, B. M. Mapping Metals Incorporation of a Whole Single Catalyst Particle Using Element Specific X-ray Nanotomography. *JACS* **2025**, *137*, 102−105, DOI: 10.1021/ja511503d.

(9) Sala, S.; Rengefors, K.; Kiventerä, J.; Patanen, M.; Gefors, L.; Werdinius, C.; Winge, S.; Broberg, K.; Kalbfleisch, S.; Sigfridsson Clauss, K. Applications of X-Ray Fluorescence Microscopy with Synchrotron Radiation: From Biology to Materials Science. *Radiat. Phys. Chem.* **2025**, *229*, No. 112491.

(10) Bossers, K. W.; Valadian, R.; Zanoni, S.; Smeets, R.; Friederichs, N.; Garrevoet, J.; Meirer, F.; Weckhuysen, B. M. Correlated X-Ray Ptychography and Fluorescence Nano-Tomography on the Fragmentation Behavior of an Individual Catalyst Particle during the Early Stages of Olefin Polymerization. *J. Am. Chem. Soc.* **2020**, *142*, 3691.

(11) Veselý, M.; Valadian, R.; Lohse, L. M.; Toepperwien, M.; Spiers, K.; Garrevoet, J.; Vogt, E. T. C.; Salditt, T.; Weckhuysen, B. M.; Meirer, F. 3-D X-Ray Nanotomography Reveals Different Carbon Deposition Mechanisms in a Single Catalyst Particle. *ChemCatChem* **2021**, *13* (10), 2494−2507.

(12) Su, B.; Li, J.; Deng, B.; Pianetta, P.; Liu, Y. Multi-Modal X-Ray Microscopy for Chemical Analysis. *TrAC Trends Anal. Chem.* **2024**, *171*, No. 117491.

(13) Zerkle, A. L.; House, C. H.; Brantley, S. L. Biogeochemical Signatures through Time as Inferred from Whole Microbial Genomes. *Am. J. Sci.* **2005**, *305*, 467−502.

(14) Simionovici, A.; Chevallier, P. 7.2 *Micro-XRF with Synchrotron Radiation*, Handbook of practical X-ray fluorescence analysis; Springer-Verlag: Berlin, Germany, 2006.

(15) Cavalazzi, B.; Lemelle, L.; Simionovici, A.; Cady, S. L.; Russell, M. J.; Bailo, E.; Canteri, R.; Enrico, E.; Manceau, A.; Maris, A.; Salomé, M.; Thomassot, E.; Bouden, N.; Tucoulou, R.; Hofmann, A. Cellular Remains in a ∼ 3.42-Billion-Year-Old Subseafloor Hydrothermal Environment. *Sci. Adv.* **2021**, *7* (29), No. eabf3963.

(16) Lepot, K.; Addad, A.; Knoll, A. H.; Wang, J.; Troadec, D.; Béché, A.; Javaux, E. J. Iron Minerals within Specific Microfossil Morphospecies of the 1.88 Ga Gunflint Formation. *Nat. Commun.* **2017**, *8* (1), No. 14890.

(17) Lemelle, L.; Simionovici, A.; Schoonjans, T.; Tucoulou, R.; Enrico, E.; Salomé, M.; Hofmann, A.; Cavalazzi, B. Analytical Requirements for Quantitative X-Ray Fluorescence Nano-Imaging of Metal Traces in Solid Samples. *TrAC Trends Anal. Chem.* **2017**, *91*, 104−111.

(18) Sforna, M. C.; Loron, C. C.; Demoulin, C. F.; François, C.; Cornet, Y.; Lara, Y. J.; Grolimund, D.; Ferreira Sanchez, D.; Medjoubi, K.; Somogyi, A.; Addad, A.; Fadel, A.; Compère, P.; Baudet, D.; Brocks, J. J.; Javaux, E. J. Intracellular Bound Chlorophyll Residues Identify 1 Gyr-Old Fossils as Eukaryotic Algae. *Nat. Commun.* **2022**, *13* (1), No. 146.

(19) Knoll, A. H.; Strother, P. K.; Rossi, S. Distribution and Diagenesis of Microfossils from the Lower Proterozoic Duck Creek Dolomite, Western Australia. *Precambrian Res.* **1988**, *38* (3), 257−279.

(20) Sasaki, K.; Ishida, A.; Takahata, N.; Sano, Y.; Kakegawa, T. Evolutionary Diversification of Paleoproterozoic Prokaryotes: New Microfossil Records in 1.88 Ga Gunflint Formation. *Precambrian Res.* **2022**, *380*, No. 106798.

(21) Barghoorn, E. S.; Tyler, S. A. Microorganisms from the Gunflint Chert. *Science* **1965**, *147*, 563−575.

(22) Alleon, J.; Bernard, S.; Le Guillou, C.; Marin-Carbonne, J.; Pont, S.; Beyssac, O.; McKeegan, K. D.; Robert, F. Molecular Preservation of 1.88 Ga Gunflint Organic Microfossils as a Function of Temperature and Mineralogy. *Nat. Commun.* **2016**, *7* (1), No. 11977.

(23) Wacey, D.; Menon, S.; Green, L.; Gerstmann, D.; Kong, C.; Mcloughlin, N.; Saunders, M.; Brasier, M. Taphonomy of Very Ancient Microfossils from the ∼ 3400Ma Strelley Pool Formation and ∼ 1900Ma Gunflint Formation: New Insights Using a Focused Ion Beam. *Precambrian Res.* **2012**, *220*−*221*, 234−250.

(24) Moreau, J. W.; Sharp, T. G. A Transmission Electron Microscopy Study of Silica and Kerogen Biosignatures in˜1.9 Ga Gunflint Microfossils. *Astrobiology* **2004**, *4* (2), 196−210.

(25) Maldanis, L.; Hickman-Lewis, K.; Verezhak, M.; Gueriau, P.; Guizar-Sicairos, M.; Jaqueto, P.; Trindade, R. I. F.; Rossi, A. L.; Berenguer, F.; Westall, F.; Bertrand, L.; Galante, D. Nanoscale 3D Quantitative Imaging of 1.88 Ga Gunflint Microfossils Reveals Novel Insights into Taphonomic and Biogenic Characters. *Sci. Rep.* **2020**, *10* (1), No. 8163.

(26) Dierolf, M.; Menzel, A.; Thibault, P.; Schneider, P.; Kewish, C. M.; Wepf, R.; Bunk, O.; Pfeiffer, F. Ptychographic X-Ray Computed Tomography at the Nanoscale. *Nature* **2010**, *467* (7314), 436−439.

(27) Karpov, D.; Cuau, L.; Shishkov, R.; Gramaccioni, C.; Dallerba, E.; Schwehr, B. J.; Cloetens, P.; Bohic, S.et al.Cryo-Correlative Light and X-ray microscopies: Expanding the Intracellular Chemical Map. *ACS Nano* 2026 DOI: 10.1021/acsnano.5c10637.

(28) Holler, M.; Diaz, A.; Guizar-Sicairos, M.; Karvinen, P.; Färm, E.; Härkönen, E.; Ritala, M.; Menzel, A.; Raabe, J.; Bunk, O. X-Ray Ptychographic Computed Tomography at 16 Nm Isotropic 3D Resolution. *Sci. Rep.* **2014**, *4* (1), No. 3857.

(29) Rodenburg, J. M.; Faulkner, H. M. L. A Phase Retrieval Algorithm for Shifting Illumination. *Appl. Phys. Lett.* **2004**, *85* (20), 4795−4797.

(30) Odstrčil, M.; Menzel, A.; Guizar-Sicairos, M. Iterative Least-Squares Solver for Generalized Maximum-Likelihood Ptychography. *Opt. Express* **2018**, *26* (3), 3108−3123.

(31) Wilke, M.; Farges, F.; Petit, P.-E.; Brown, G. E.; Martin, F. Oxidation State and Coordination of Fe in Minerals: An Fe K-XANES Spectroscopic Study. *Am. Mineral.* **2001**, *86* (5−6), 714−730.

(32) Solé, V.; Papillon, E.; Cotte, M.; Walter, Ph.; Susini, J. A Multiplatform Code for the Analysis of Energy-Dispersive X-Ray Fluorescence Spectra. *Spectrochim. Acta, Part B* **2007**, *62* (1), 63−68.

(33) Shapiro, R. S.; Konhauser, K. O. Hematite-Coated Microfossils: Primary Ecological Fingerprint or Taphonomic Oddity of the Paleoproterozoic? *Geobiology* **2015**, *13* (3), 209−224.

(34) Johnson, J. E. *Low-Fe(III) Greenalite Was a Primary Mineral from Neoarchean Oceans (Raw Data)*; University of Michigan - Deep Blue Data DOI: 10.7302/Z2XS5SMK.

(35) Sanchez, D. F.; Simionovici, A. S.; Lemelle, L.; Cuartero, V.; Mathon, O.; Pascarelli, S.; Bonnin, A.; Shapiro, R.; Konhauser, K.; Grolimund, D.; Bleuet, P. 2D/3D Microanalysis by Energy Dispersive X-Ray Absorption Spectroscopy Tomography. *Sci. Rep.* **2017**, *7* (1), No. 16453.

(36) Rasmussen, B.; Muhling, Jr.; Fischer, Ww. Ancient Oil as a Source of Carbonaceous Matter in 1.88-Billion-Year-Old Gunflint Stromatolites and Microfossils. *Astrobiology* **2021**, *21* (6), 655−672.

(37) Phoenix, V. R.; Adams, D. G.; Konhauser, K. O. Cyanobacterial Viability during Hydrothermal Biomineralisation. *Chem. Geol.* **2000**, *169* (3), 329−338.

(38) Diaz, A.; Trtik, P.; Guizar-Sicairos, M.; Menzel, A.; Thibault, P.; Bunk, O. Quantitative X-Ray Phase Nanotomography. *Phys. Rev. B* **2012**, *85* (2), No. 020104.

(39) Loferer-Krößbacher, M.; Klima, J.; Psenner, R. Determination of Bacterial Cell Dry Mass by Transmission Electron Microscopy and Densitometric Image Analysis. *Appl. Environ. Microbiol.* **1998**, *64* (2), 688−694.

(40) Glass, J. B.; Chen, S.; Dawson, K. S.; Horton, D. R.; Vogt, S.; Ingall, E. D.; Twining, B. S.; Orphan, V. J. Trace Metal Imaging of Sulfate-Reducing Bacteria and Methanogenic Archaea at Single-Cell Resolution by Synchrotron X-Ray Fluorescence Imaging. *Geomicrobiol. J.* **2018**, *35* (1), 81−89.

(41) Outten, C. E.; O'Halloran, T. V. Femtomolar Sensitivity of Metalloregulatory Proteins Controlling Zinc Homeostasis. *Science* **2001**, *292* (5526), 2488−2492.

(42) Keren, N.; Aurora, R.; Pakrasi, H. B. Critical Roles of Bacterioferritins in Iron Storage and Proliferation of Cyanobacteria. *Plant Physiol.* **2004**, *135* (3), 1666−1673.

(43) Fiedor, J.; Ostachowicz, B.; Baster, M.; Lankosz, M.; Burda, K. Quantification of Purple Non-Sulphur Phototrophic Bacteria and Their Photosynthetic Structures by Means of Total Reflection X-Ray Fluorescence Spectrometry (TXRF). *J. Anal. At. Spectrom.* **2016**, *31* (10), 2078−2088.

(44) Büttner, M.; Xie, D. L.; Nelson, H.; Pinther, W.; Hauska, G.; Nelson, N. Photosynthetic Reaction Center Genes in Green Sulfur Bacteria and in Photosystem 1 Are Related. *Proc. Natl. Acad. Sci. U.S.A.* **1992**, *89* (17), 8135−8139.

(45) Saito, M. A.; Bertrand, E. M.; Dutkiewicz, S.; Bulygin, V. V.; Moran, D. M.; Monteiro, F. M.; Follows, M. J.; Valois, F. W.; Waterbury, J. B. Iron Conservation by Reduction of Metalloenzyme Inventories in the Marine Diazotroph *Crocosphaera Watsonii*. *Proc. Natl. Acad. Sci. U.S.A.* **2011**, *108* (6), 2184−2189.

(46) Keren, N.; Kidd, M. J.; Penner-Hahn, J. E.; Pakrasi, H. B. A Light-Dependent Mechanism for Massive Accumulation of Manganese in the Photosynthetic Bacterium Synechocystis Sp. PCC 6803. *Biochemistry* **2002**, *41* (50), 15085−15092.

(47) Jones, G. E.; Royle, L. G.; Murray, L. Cationic Composition of 22 Species of Bacteria Grown in Seawater Medium. *Appl. Environ. Microbiol.* **1979**, *38* (5), 800−805.

(48) Lukmanov, R. A.; Tulej, M.; Ligterink, N. F. W.; De Koning, C.; Riedo, A.; Grimaudo, V.; Neubeck, A.; Wacey, D.; Wurz, P. Chemical Identification of Microfossils from the 1.88-Ga Gunflint Chert: Towards Empirical Biosignatures Using Laser Ablation Ionization Mass Spectrometer. *J. Chemom.* **2021**, *35* (10), No. e3370.

(49) Golosio, B.; Simionovici, A.; Somogyi, A.; Lemelle, L.; Chukalina, M.; Brunetti, A. Internal Elemental Microanalysis Combining X-Ray Fluorescence, Compton and Transmission Tomography. *J. Appl. Phys.* **2003**, *94* (1), 145−156.

(50) Gräfenstein, A.; Brückner, D.; Rumancev, C.; Garrevoet, J.; Galbierz, V.; Schroeder, W. H.; Schroer, C. G.; Falkenberg, G.; Rosenhahn, A. Single-Slice XRF Mapping of Light Elements in Frozen-Hydrated Allium Schoenoprasum via a Self-Absorption-Corrected Hyperspectral Tomographic Reconstruction Approach. *Anal. Chem.* **2023**, *95* (27), 10186−10195.

(51) Shishkov, R.; Laugros, A.; Vigano, N.; Bohic, S.; Karpov, D.; Cloetens, P. Self-Supervised Deep-Learning Denoising for X-ray Fluorescence Microscopy with Multi-Element Detectors. *Anal. Chem.* **2026**, DOI: 10.1021/acs.analchem.5c05552.

(52) Dong, M.; Yang, W.; Hao, J.; Jia, X.; Yang, O.; Lo, M. K. F.; Cao, B.; Hu, S.; Lin, Y. Cross-Scale Multimodal Imaging for Organic Matter in Extraterrestrial Samples. *Anal. Chem.* **2025**, *97* (15), 8258−8267.